Pet. Sci. (2017) 14:694–710
DOI 10.1007/s12182-017-0191-0

ORIGINAL PAPER

Bayesian seismic multi-scale inversion in complex Laplace mixed domains

Kun Li[1] · Xing-Yao Yin[1,2] · Zhao-Yun Zong[1,2]

Received: 19 February 2017 / Published online: 20 October 2017

Abstract Seismic inversion performed in the time or frequency domain cannot always recover the long-wavelength background of subsurface parameters due to the lack of low-frequency seismic records. Since the low-frequency response becomes much richer in the Laplace mixed domains, one novel Bayesian impedance inversion approach in the complex Laplace mixed domains is established in this study to solve the model dependency problem. The derivation of a Laplace mixed-domain formula of the Robinson convolution is the first step in our work. With this formula, the Laplace seismic spectrum, the wavelet spectrum and time-domain reflectivity are joined together. Next, to improve inversion stability, the object inversion function accompanied by the initial constraint of the linear increment model is launched under a Bayesian framework. The likelihood function and prior probability distribution can be combined together by Bayesian formula to calculate the posterior probability distribution of subsurface parameters. By achieving the optimal solution corresponding to maximum posterior probability distribution, the low-frequency background of subsurface parameters can be obtained successfully. Then, with the regularization constraint of estimated low frequency in the Laplace mixed domains, multi-scale Bayesian inversion in the pure frequency domain is exploited to obtain the absolute model parameters. The effectiveness, anti-noise capability and lateral continuity of Laplace mixed-domain inversion are illustrated by synthetic tests. Furthermore, one field case in the east of China is discussed carefully with different input frequency components and different inversion algorithms. This provides adequate proof to illustrate the reliability improvement in low-frequency estimation and resolution enhancement of subsurface parameters, in comparison with conventional Bayesian inversion in the frequency domain.

Keywords Low-frequency · Complex mixed-domain · Laplace inversion · Bayesian estimation · Multi-scale inversion

1 Introduction

There are many ill-conditioned geophysical inversion problems in geophysical prospecting due to the absence of sufficient field data. So their solutions may become unstable or non-unique. Although there has been enormous development in seismic acquisition technology to achieve the acquisition of broadband seismic signals (Day et al. 2013; Kroode et al. 2013; Haavik and Landrø 2015), the signal-to-noise ratio (SNR) of low- and high-frequency components is also controversial topics, specifically for frequencies lower than 2–5 Hz and higher than 100 Hz. However, low frequencies play an important role in seismic exploration, especially for resolution enhancement, better imaging quality, effective inversion processes and direct fluid identification. As we know, the width of the main lobe of the wavelet depends on the relative high-frequency

✉ Xing-Yao Yin
xyyin@upc.edu.cn

[1] School of Geosciences, China University of Petroleum (East China), Qingdao 266580, Shandong, China

[2] Laboratory for Marine Mineral Resources, Qingdao National Laboratory for Marine Science and Technology, Qingdao 266071, Shandong, China

Edited by Jie Hao

energy and broadening the low-frequency bandwidth can effectively reduce the amplitude of wavelet side lobes (Kroode et al. 2013; Liu et al. 2013). Considering the influence of low frequencies on seismic imaging and velocity analysis in contrast to high frequencies, less absorption, less scattering and better penetration of low frequencies illustrate their importance in the field of deep imaging technology (Pedersen and Becken 2005; Spjuth et al. 2012; Cao and Chen 2014; Zhang et al. 2015). Geophysicists still prioritize low-frequency regularizations in waveform, impedance, elastic and AVO inversion (Zong et al. 2012; Kroode et al. 2013; Li et al. 2016a) to improve the stability of the inversion process and the rate of convergence to a precise earth model. Low-frequency shadows under hydrocarbon reservoirs (Chabyshova and Goloshubin 2014; Zhang et al. 2014; Yin et al. 2015a; Li et al. 2016b) and fluid mobility measurements of the saturated reservoir based on low frequencies (Chen et al. 2012; Yin et al. 2015a) are also two important frequency-dependent seismic attributes to describe reservoir characteristics.

Due to the deficiency of field data, many regularization terms are applied to decrease the problem about the lack of low- and high-frequency components, such as prior information on model parameters, bounding and geological constraints (Tarantola 2005; Kim and Kim 2011; Zhang et al. 2013; Yuan and Wang 2013; Hamid and Pidlisecky 2015; Yin et al. 2013, 2015b; Zong et al. 2015; Liu et al. 2016; Li et al. 2016a). The above-mentioned methods only account for overcoming multiple solutions and avoiding unrealistic values of the local minima in the objective function. Among all influence factors, the background of estimated parameters is seriously dependent on the accuracy of the initial model, which plays an important role in supplementing the low-frequency components of conventional seismic inversion. Therefore, selecting a suitable initial model can enhance the convergence rate and increase the estimation reliability in seismic inversion (Shin and Cha 2008; Zong et al. 2016; Yin et al. 2016; Li et al. 2016b). However, the reliable prior information of subsurface parameters cannot always be established in some cases, such as in a well-less exploration field, which will increase the difficulty in seismic inversion and interpretation works.

To mitigate the model-dependent problem of seismic inversion, geophysicists have attempted to deploy inversion without a precise preliminary model and exploit the limited data to derive the ultra-low-frequency information of our interested parameters. As we all know, if the damping effect is appended in the pure frequency domain, one novel inversion strategy in the complex frequency domain is yielded, which can alleviate the ill-conditioned problem of band-limited inversion slightly (Sirgue and Pratt 2004). Shin and Cha (2008) proposed a waveform inversion algorithm based on the zero-frequency component of the damped wave field in the pure Laplace domain to recover the long-wavelength velocity models. Due to the algorithm's drawback of penetration depth, the complex Laplace–Fourier-domain inversion strategy was proposed (Shin and Cha 2009; Ha and Shin 2012, 2013; Hu et al. 2015) via a series of low-frequency components within 5 Hz and damping constants, which can enlarge the input energy and improve the penetration depth of subsurface models. Recently, seismic envelope inversion that was performed in the envelope domain to predict the low-frequency background of subsurface velocity by synthesizing the envelope's misfit function has attracted the attention of geophysicists (Wu et al. 2014; Luo and Wu 2015; Luo et al. 2016). Complex Laplace-domain inversion and envelope inversion are two different representatives of low-frequency estimation methods, but both aim at excavating the low-frequency response from the original data and improving the construction of low-frequency a priori information of the ill-posed inverse problem.

Based on the previous research in low-frequency inversion, we propose a novel Bayesian impedance inversion method in the Laplace mixed domains, which is not dependent on the precision of the initial model. Margrave (1998) proposed the Fourier mixed-domain formulation of a non-stationary convolution model when studying the time-variant deconvolution in the frequency domain. In this paper, the deduction of the Laplace mixed-domain formula of the convolution model is the first step of our method, which is comprised of the Laplace seismic spectrum, the wavelet spectrum and time-domain reflectivity. Furthermore, the Bayesian estimation system is lodged in our inversion process to enhance the stability and resolution of estimated parameters. For the next step, the object function of complex Laplace mixed-domain inversion can be established, accompanied by the linear increment initial model of subsurface parameters with L2-norm regularization. Furthermore, the feasibility of complex Laplace mixed-domain inversion and multi-scale strategy is demonstrated by the 1D synthetic and 2D overthrust model tests. Finally, one successful field case with the proposed method is displayed, and the results illustrate its great potential for low-frequency recovery and high-resolution estimation.

2 Laplace mixed-domain seismic model

The Laplace transform can be considered as the Fourier transform of the damped time-domain signal. Assuming the time-domain signal $y(t)$, the Laplace transformation of $y(t)$ can be stated as,

$$Y(s) = \int_0^{+\infty} y(t)\mathrm{e}^{-st}\mathrm{d}t = \int_0^{+\infty} y(t)\mathrm{e}^{-\sigma t}\mathrm{e}^{-i2\pi ft}\mathrm{d}t \tag{1}$$

where $Y(s)$, σ and s are the Laplace spectrum of the input signal, damping coefficients and complex frequency, respectively. Here, s can be expressed as $\sigma + i2\pi f$. By substituting Robinson stationary convolution for $y(t)$ in Eq. (1), Eq. (1) can be rewritten as,

$$Y(\sigma + i2\pi f) = \int_0^{+\infty} \left[\int_0^{+\infty} w(t-\tau)m(\tau)\mathrm{d}\tau\right]\mathrm{e}^{-\sigma t}\mathrm{e}^{-i2\pi ft}\mathrm{d}t \tag{2}$$

where $w(t-\tau)$ represents the band-limited seismic wavelet and $m(\tau)$ shows the underground reflectivity. Then, interchanging the order of integration of Eq. (2), it can be rewritten as

$$Y(\sigma + i2\pi f) = \int_0^{+\infty} \left[\int_0^{+\infty} w(t-\tau)\mathrm{e}^{-\sigma t}\mathrm{e}^{-i2\pi ft}\mathrm{d}t\right] \cdot m(\tau)\mathrm{d}\tau \tag{3}$$

According to the time-shifting property of the Laplace transform, the final Laplace mixed-domain equation of time-domain convolution can be written as

$$Y(\sigma + i2\pi f) = W(\sigma + i2\pi f)\int_0^{+\infty} m(\tau)\cdot \mathrm{e}^{-\sigma\tau}\mathrm{e}^{-i2\pi f\tau}\mathrm{d}\tau \tag{4}$$

where $W(\sigma + i2\pi f)$ indicates the Laplace spectrum of the time-domain wavelet. The natural exponential term $\mathrm{e}^{-\sigma\tau}\cdot\mathrm{e}^{-i2\pi f\tau}$ refers to the time-shifting operator or Laplace operator. To see the significance of the Laplace–Fourier transformation more precisely, the damped wavelets (20 Hz) and synthetic seismic in the time domain with a series of damping parameters are displayed in Fig. 1. The damped wavelets corresponding to damping constants 0, 8 and 16 s^{-1} are shown in Fig. 1a–c. The damped synthetics with previous damping constants are shown in Fig. 1d–f. In Figs. 2 and 3, the Laplace–Fourier spectra of a 20-Hz Ricker wavelet and synthetic seismic are displayed in detail. In Fig. 1, we can see that the damped wavelets behave asymmetrically along with variations of attenuation values, especially with a large damping coefficient 16 s^{-1}; this is caused by asymmetric attenuation of the Laplace transform. Similarly, the deep attenuation effects of seismic signals are stronger than shallow attenuation. From the contour maps of the Laplace spectrum in Fig. 2, the energy of low frequencies has a strong increase variation below 2.0 Hz, which deviates from the normal decrease tendency at high frequencies. The magnitudes of the Laplace spectrum indicate that the energy below 2.0 Hz increases gradually with variations of Laplace damping coefficients under the condition of $\sigma < 30$, which is described in Fig. 3a, b more clearly (i.e., the low-frequency components are amplified with the Laplace damping coefficients). The tremendous variations may increase the weights of low frequencies and lead us to recover much richer low-frequency responses of a subsurface model in complex Laplace-domain inversion than conventional time-domain and frequency-domain inversion.

3 Impedance inversion in the Laplace mixed domains

To discuss the inverse problem more clearly, Eq. (4) is simplified and a constant angular frequency ω_j is assumed, so the discrete matrix equation of Eq. (4) can be given as,

$$\mathbf{Y}_{\omega_j} = \mathbf{W}_{\omega_j}\cdot\mathbf{C}\cdot\mathbf{E}_{\omega_j}\cdot\mathbf{m} \tag{5}$$

where $\mathbf{W}_{\omega_j}$, $\mathbf{C}$ and $\mathbf{E}_{\omega_j}$ are the Laplace spectrum of wavelets, damping matrix of subsurface reflectivity corresponding to each sample and Fourier forwarding matrix, respectively. $\mathbf{Y}_{\omega_j}$ is the vector of the input Laplace seismic spectrum, and $\mathbf{m}$ is the vector of interested parameters. The Laplace spectrum of wavelets can be written as a diagonal matrix,

$$\mathbf{W}_{\omega_j} = \begin{bmatrix} W(\sigma_1 + i\omega_j) & 0 & \cdots & 0 \\ 0 & W(\sigma_2 + i\omega_j) & \cdots & 0 \\ \vdots & \vdots & \ddots & \vdots \\ 0 & 0 & \cdots & W(\sigma_k + i\omega_j) \end{bmatrix}_{k\times k} \tag{6}$$

In Eq. (6), k is assumed to be the number of damping coefficients, and the Laplace damping matrix can be stated as,

$$\mathbf{C} = \begin{bmatrix} \mathrm{e}^{-\tau_1\sigma_1} & \mathrm{e}^{-\tau_2\sigma_1} & \cdots & \mathrm{e}^{-\tau_n\sigma_1} \\ \mathrm{e}^{-\tau_1\sigma_2} & \mathrm{e}^{-\tau_2\sigma_2} & \cdots & \mathrm{e}^{-\tau_n\sigma_2} \\ \vdots & \vdots & \ddots & \vdots \\ \mathrm{e}^{-\tau_1\sigma_k} & \mathrm{e}^{-\tau_2\sigma_k} & \cdots & \mathrm{e}^{-\tau_n\sigma_k} \end{bmatrix}_{k\times n} \tag{7}$$

where n is the number of time samples and τ_n is the time index. The input of damping coefficients σ in matrix $\mathbf{C}$ plays important role in the estimation of low frequency. The discrete Fourier forwarding matrix $\mathbf{E}_{\omega_j}$ can be given as,

$$\mathbf{E}_{\omega_j} = \begin{bmatrix} \mathrm{e}^{-i\tau_1\omega_j} & 0 & \cdots & 0 \\ 0 & \mathrm{e}^{-i\tau_2\omega_j} & \cdots & 0 \\ \vdots & \vdots & \ddots & \vdots \\ 0 & 0 & \cdots & \mathrm{e}^{-i\tau_n\omega_j} \end{bmatrix}_{n\times n} \tag{8}$$

By assuming the number of selected frequencies as l, joining Eqs. (5)–(8) can yield the forward equation easily as,

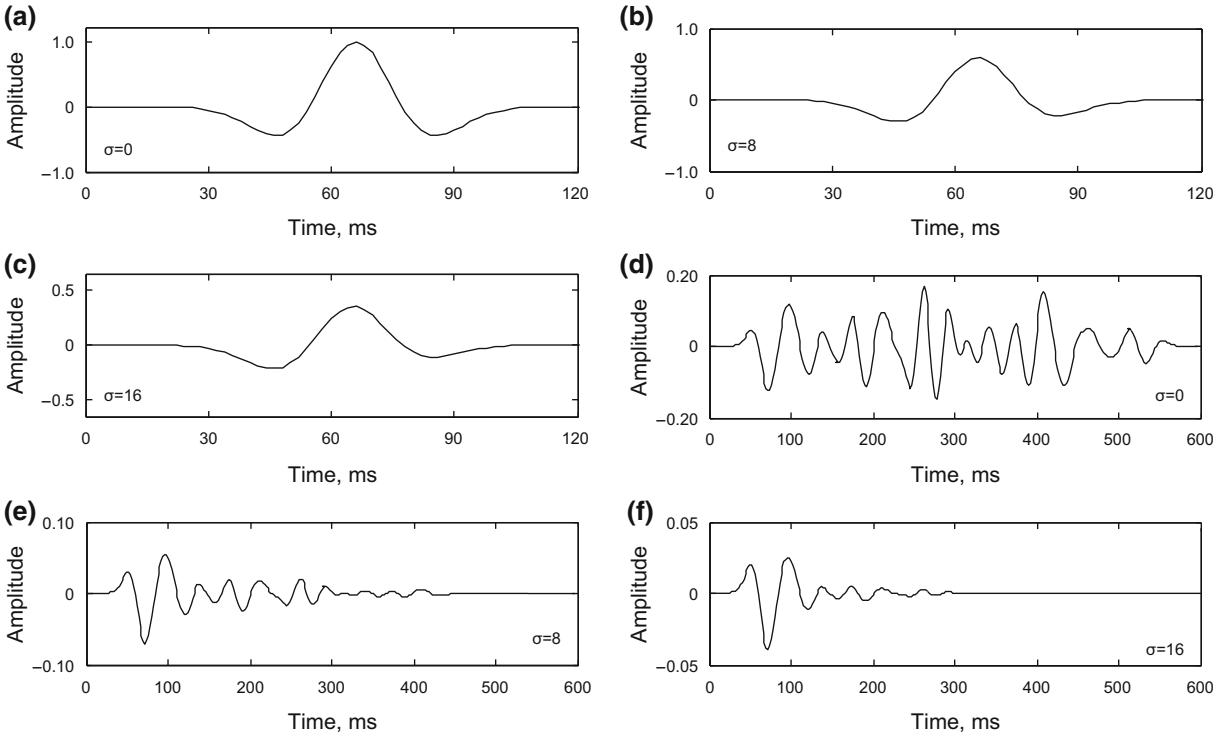

Fig. 1 Damped wavelets (20.0 Hz) and synthetic seismic in the time domain with a series of damping parameters. **a–c** are damped wavelets corresponding to damping constants 0, 8 and 16 s^{-1}, respectively, and **d–f** are damped synthetic data corresponding to damping constants 0, 8 and 16 s^{-1}, respectively

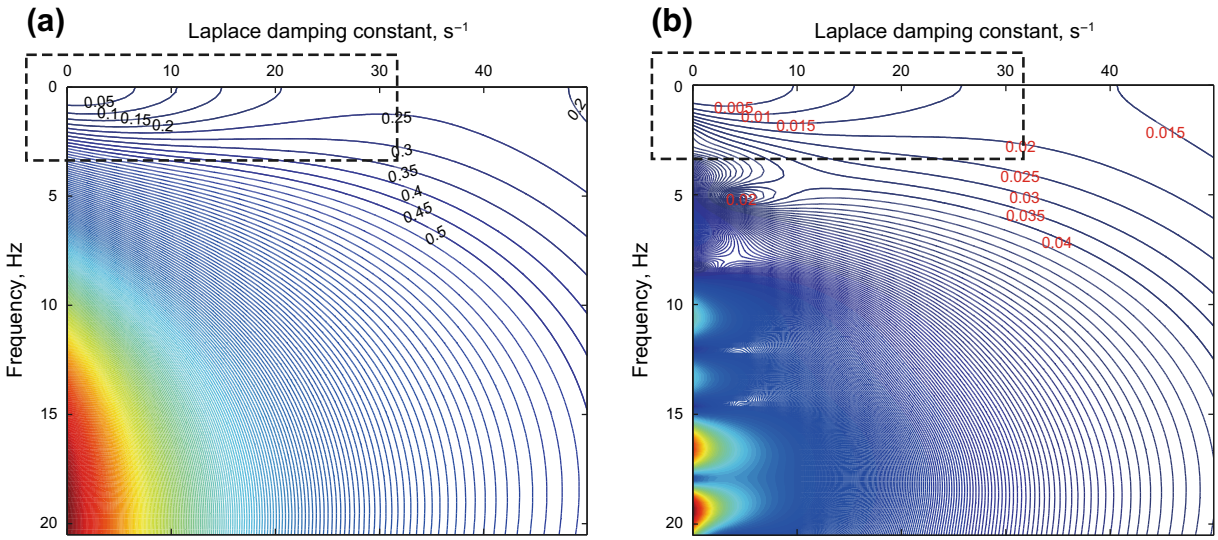

Fig. 2 Laplace–Fourier spectra of 20-Hz Ricker wavelet and synthetic seismic. **a** Wavelet spectrum and **b** seismic spectrum

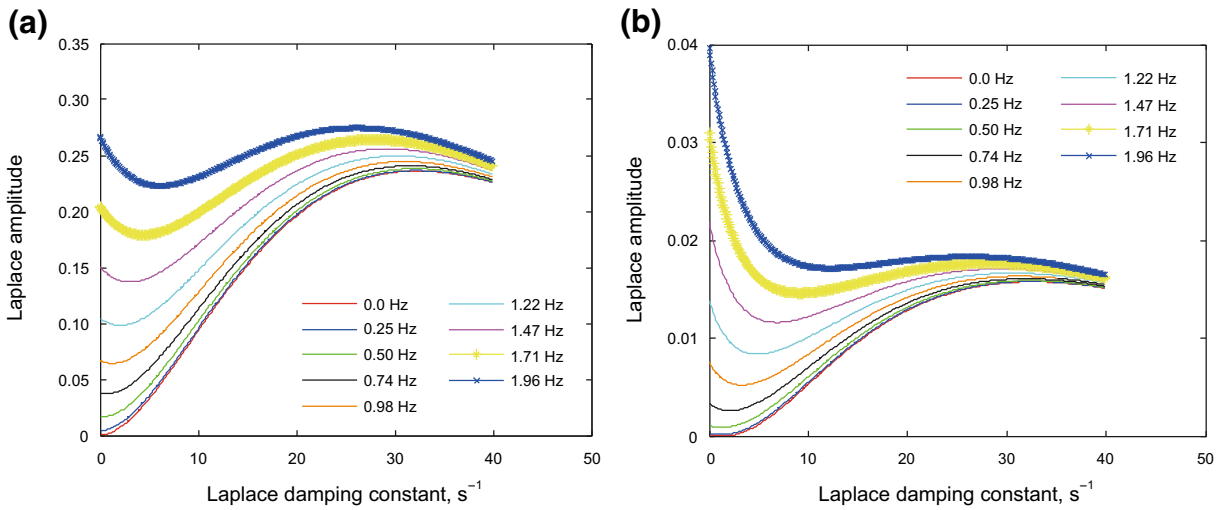

Fig. 3 Amplification of low-frequency components with a variation in Laplace damping coefficients. **a** Wavelet spectrum and **b** seismic spectrum

$$\underbrace{\begin{bmatrix}\mathbf{Y}_{\omega_1}\\ \mathbf{Y}_{\omega_2}\\ \vdots\\ \mathbf{Y}_{\omega_l}\end{bmatrix}_{kl}}_{\mathbf{Y}} = \underbrace{\begin{bmatrix}\mathbf{W}_{\omega_1}\cdot\mathbf{C} & 0 & \vdots & 0\\ 0 & \mathbf{W}_{\omega_2}\cdot\mathbf{C} & \vdots & \vdots\\ \vdots & \vdots & \ddots & 0\\ 0 & 0 & 0 & \mathbf{W}_{\omega_l}\cdot\mathbf{C}\end{bmatrix}_{kl\times nl}}_{\mathbf{G}} \underbrace{\begin{bmatrix}\mathbf{E}_{\omega_1}\\ \mathbf{E}_{\omega_2}\\ \vdots\\ \mathbf{E}_{\omega_l}\end{bmatrix}_{nl\times n}}_{\mathbf{E}} \cdot\mathbf{m} \tag{9}$$

where $\mathbf{Y}$ is the complex Laplace seismic spectrum, $\mathbf{G}$ is the product of the wavelet matrix $\mathbf{W}_{\omega_i}$ and attenuation matrix $\mathbf{C}$ and $\mathbf{E}$ is the Fourier operator of the multi-frequency components. Due to the complexity of Eq. (9), we can rewrite it in real and imaginary parts as follows,

$$\begin{bmatrix}\text{real}(\mathbf{Y})\\ \text{imag}(\mathbf{Y})\end{bmatrix} = \begin{bmatrix}\text{real}(\mathbf{G}\cdot\mathbf{E})\\ \text{imag}(\mathbf{G}\cdot\mathbf{E})\end{bmatrix}\cdot\mathbf{m} \tag{10}$$

Supposing $\mathbf{S}' = [\text{real}(\mathbf{Y}) \quad \text{imag}(\mathbf{Y})]^{\mathrm{T}}$, the real operator $\mathbf{G}'\mathbf{L}' = [\text{real}(\mathbf{G}\cdot\mathbf{E}) \quad \text{imag}(\mathbf{G}\cdot\mathbf{E})]^{\mathrm{T}}$ in Eq. (10), it can be written as a simplified form,

$$\mathbf{S}' = \mathbf{G}'\cdot\mathbf{L}'\cdot\mathbf{m} \tag{11}$$

where $\mathbf{S}'$, $\mathbf{G}'$ and $\mathbf{L}'$ represent the Laplace seismic spectrum, wavelet effect and Laplace effect, respectively. It is worth noting that the input spectrum $\mathbf{Y}_{\omega_j}$ is one real vector when the input frequency ω_j is equal to zero. Fourier-domain inversion is the special case of Laplace-domain inversion when there is no input for attenuation coefficients σ. In other words, Laplace-domain inversion is an extension of Fourier-domain inversion. Besides, the selections of discrete frequency components and Laplace damping constants are pivotal problems that can influence the penetration depth of the underground model (Shin and Cha 2008, 2009; Li et al. 2016a).

4 Inversion strategy based on the Bayesian system

For the regularization algorithm in Laplace mixed-domain inversion, one robust Laplace mixed-domain multi-scale inversion based on a Bayesian framework is proposed. The introduction of the model parameter's priori information into mixed-domain inversion can help to improve the stability and anti-noise ability of the proposed approach. Assuming that the probability distribution of random noise $\mathbf{S}' - \mathbf{G}'\mathbf{L}'\mathbf{m}$ in the Laplace domain obeys a Gaussian function and Gaussian probability is taken as the likelihood function $p_{\text{Gauss}}(\mathbf{S}'|\mathbf{m})$, which describes the fitting degree between the synthetic and real Laplace spectrum, as mentioned here,

$$p_{\text{Gauss}}(\mathbf{S}'|\mathbf{m}) = \frac{1}{(2\pi\sigma_n^2)^{kl}} \exp[-(\mathbf{S}' - \mathbf{G}'\mathbf{L}'\mathbf{m})^{\mathrm{T}}(\mathbf{S}' - \mathbf{G}'\mathbf{L}'\mathbf{m})/2\sigma_n^2] \tag{12}$$

where σ_n^2 is the variance of the residual Laplace spectrum $(\mathbf{S}' - \mathbf{G}'\mathbf{L}'\mathbf{m})$ between synthetic and real seismic profiles. Since the mixed-domain convolution contains time-domain reflectivity, we can easily introduce the available prior information on estimated parameters to reduce the multiple solutions of the proposed method. However, the optimum solution corresponding to Gaussian prior probability lacks anti-noise performance and does not realize high-resolution results of subsurface parameters (Alemie and Sacchi 2011). Because the Cauchy probability distribution of the model parameters has long tails compared to the Gaussian probability distribution, it can suppress weak noise and highlight large reflectivity at the same time. The different weighting coefficients on constrained parameters of

Cauchy regularization can achieve sparse solutions and stable results (Downton 2005; Buland and Omre 2003). So we introduced the Cauchy prior function $\boldsymbol{p}_{\text{Cauchy}}(\mathbf{m})$ to our Laplace mixed-domain inversion in this paper. The explicit expression of the Cauchy function can be stated as (Downton 2005; Yang 2008; Alemie and Sacchi 2011; Zong et al. 2015; Li et al. 2016a),

$$p_{\text{Cauchy}}(\mathbf{m}) = \frac{1}{(\pi\sigma_m)^n}\prod_{i=1}^{n}\left[1 + m_i^2/\sigma_m^2\right]^{-1} \tag{13}$$

where σ_m^2 is the variance of time-domain model parameters and m_i represents the discrete reflectivity. The likelihood function and prior Cauchy regularization can be linked together effectively by a Bayesian framework (Yang et al. 2015; Yin et al. 2016), which can be expressed by the conditional probability formula,

$$\begin{aligned} p(\mathbf{m}|\mathbf{S}') &= \frac{p_{\text{Cauchy}}(\mathbf{m})p_{\text{Gauss}}(\mathbf{S}'|\mathbf{m})}{\int p(\mathbf{m})p(\mathbf{S}'|\mathbf{m})\mathrm{d}(\mathbf{m})} \\ &\propto p_{\text{Cauchy}}(\mathbf{m})p_{\text{Gauss}}(\mathbf{S}'|\mathbf{m}) \end{aligned} \tag{14}$$

Then, the posterior probability distribution $p(\mathbf{m}|\mathbf{S}')$ can be obtained by Eq. (14), so substituting Eqs. (12) and (13) for Eq. (14) yields,

$$\begin{aligned} p(\mathbf{m},\sigma_n|\mathbf{S}') &\propto \exp\left[-\sum_{1}^{n}\ln\left(1 + m_i^2/\sigma_m^2\right)\right] \\ &\times \exp[-(\mathbf{S}' - \mathbf{G}'\mathbf{L}'\mathbf{m})^{\mathrm{T}}(\mathbf{S}' - \mathbf{G}'\mathbf{L}'\mathbf{m})\Big/2\sigma_n^2] \end{aligned} \tag{15}$$

Due to the monotonic increasing property of the exponential function exp[], the equivalent form of Eq. (15) can be expressed as

$$\begin{aligned} \ln[p(\mathbf{m},\sigma_n|\mathbf{S}')] \propto &-(\mathbf{S}' - \mathbf{G}'\mathbf{L}'\mathbf{m})^{\mathrm{T}}(\mathbf{S}' - \mathbf{G}'\mathbf{L}'\mathbf{m}) \\ &- 2\sigma_n^2\sum_{i=1}^{n}\ln\left(1 + m_i^2/\sigma_m^2\right) \end{aligned} \tag{16}$$

If we expect the optimum solution corresponding to maximum posterior probability (MAP), the derivative of $\ln[\boldsymbol{p}(\mathbf{m},\sigma_n|\mathbf{S}')]$ can be stated as,

$$\begin{aligned} \frac{\partial \ln[p]}{\partial \mathbf{m}} = &[\mathbf{G}'\mathbf{L}']^{\mathrm{T}}[\mathbf{G}'\mathbf{L}']\mathbf{m} - [\mathbf{G}'\mathbf{L}']^{\mathrm{T}}\mathbf{S}' \\ &+ 4\frac{\sigma_n^2}{\sigma_m^2}\mathrm{diag}\left(\left[1 + m_i^2/\sigma_m^2\right]^{-1}\right)\mathbf{m} \end{aligned} \tag{17}$$

Supposing that $\frac{\partial \ln[p]}{\partial \mathbf{m}}$ is equal to zero, the following equation is yielded,

$$\mathbf{m} = \left([\mathbf{G}'\mathbf{L}']^{\mathrm{T}}[\mathbf{G}'\mathbf{L}'] + 4\frac{\sigma_n^2}{\sigma_m^2}\mathbf{Q}\right)^{-1}\left([\mathbf{G}'\mathbf{L}']^{\mathrm{T}}\mathbf{S}'\right) \tag{18}$$

where $\mathbf{Q}$ is the regularized diagonal matrix and each coefficient of $\mathbf{Q}$ is equal to $[1 + m_i^2/\sigma_m^2]^{-1}$. Due to the ill-posed property of the seismic inverse problem, the constraint of the linear background ς on model parameters is introduced, which can be stated by L2-norm regularization (Li et al. 2016a; Yin et al. 2016),

$$J_{\text{pri}}(\mathbf{m}) = \mathbf{L}_2^2[\varsigma - \mathbf{D}\cdot\mathbf{m}] = \|\varsigma - \mathbf{D}\cdot\mathbf{m}\|_2^2 \tag{19}$$

where $\mathbf{D}$ is the regularized integral matrix and ς is the relative impedance that is equal to $0.5 \times \ln[IP_i/IP_0]$, where IP_0 is the reference impedance value. With the combination of Eq. (18) and the prior background constraint (19), we obtain the final inversion function as

$$\begin{aligned} \mathbf{m} = &\left([\mathbf{G}'\mathbf{L}']^{\mathrm{T}}\cdot[\mathbf{G}'\mathbf{L}'] + 4\frac{\sigma_n^2}{\sigma_m^2}\mathbf{Q} + \varepsilon^2\mathbf{D}^{\mathrm{T}}\mathbf{D}\right)^{-1} \\ &\cdot\left([\mathbf{G}'\mathbf{L}']^{\mathrm{T}}\cdot\mathbf{S}' + \varepsilon^2\mathbf{D}^{\mathrm{T}}\varsigma\right) \end{aligned} \tag{20}$$

Here, ε^2 is the positive regularization parameter, which is used to characterize the weight of the prior information constraint in the proposed algorithm. When the seismic data are seriously disturbed by random noise (low *S/N*), the regularization parameter ε^2 should be increased appropriately, otherwise conversely. For the nonlinear Eq. (20), iterative reweighted least squares are applied to solve the inverse problem (Tarantola 2005; Yang 2008). Once the relative reflectivity is achieved, the absolute impedance IP_i can be obtained with the integral operation. For the resolution enhancement and convergence precision of seismic inversion, the multi-scale inversion strategy with multi-component successive iterations in the pure frequency domain is utilized to obtain the final subsurface parameters after low-frequency estimation in the Laplace mixed domains.

5 Methodology tests

5.1 1D synthetic tests

To illustrate the effectiveness of the Laplace mixed-domain inversion, we first investigated the inversion algorithm on 1D synthetic data. Figure 4 demonstrates the seismic gathers that were generated with resampling well-logging impedance and one 20-Hz band-limited Ricker wavelet of zero phase. The conventional estimated results shown in Fig. 5 without the low-frequency constraints show strong errors from the theoretical model, especially on the background of model parameters, which can be seen clearly at the black ellipses. Figures 6, 7, 8 and 9 show the predicted parameters with the proposed method under different noise contaminations. In Figs. 5, 6, 7, 8 and 9, blue lines refer to the original model, green lines refer to the linear initial model and red refers to the predicted parameters. With specific analysis from Fig. 6, we can discover that Laplace

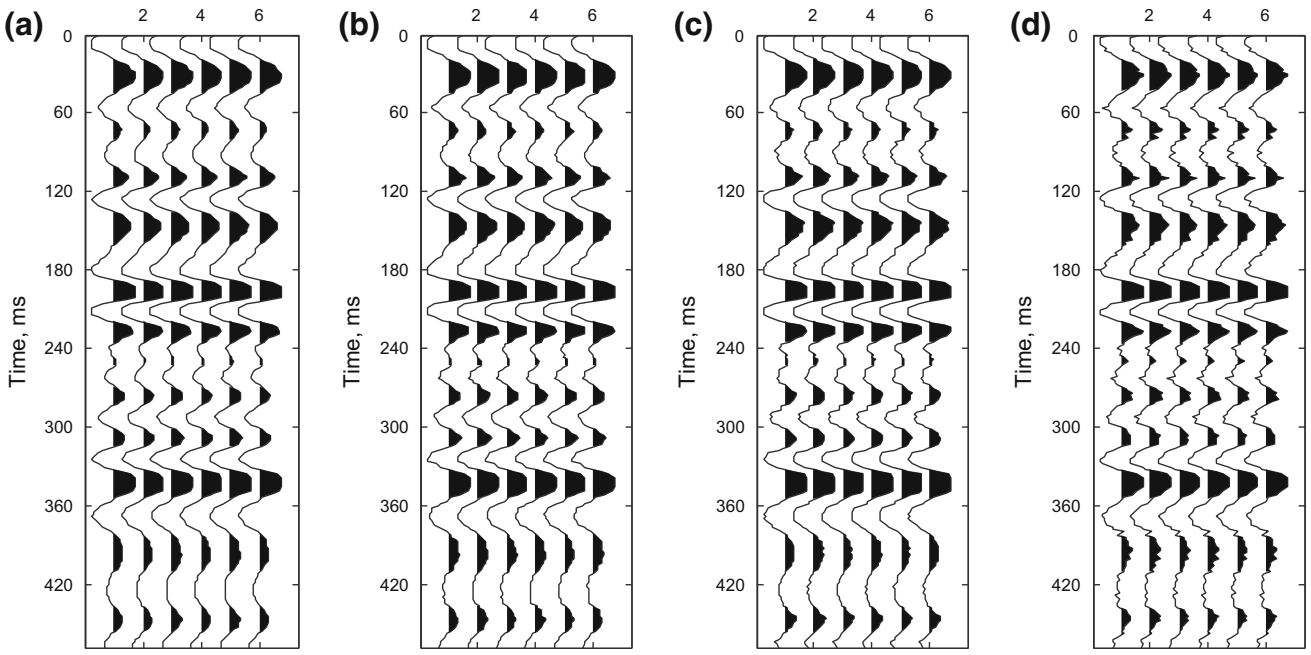

Fig. 4 Synthetic gathers under different noise levels utilizing a known well W and a 20-Hz Ricker wavelet. **a** Noise-free, **b** $S/N = 20$, **c** $S/N = 10$, and **d** $S/N = 5$

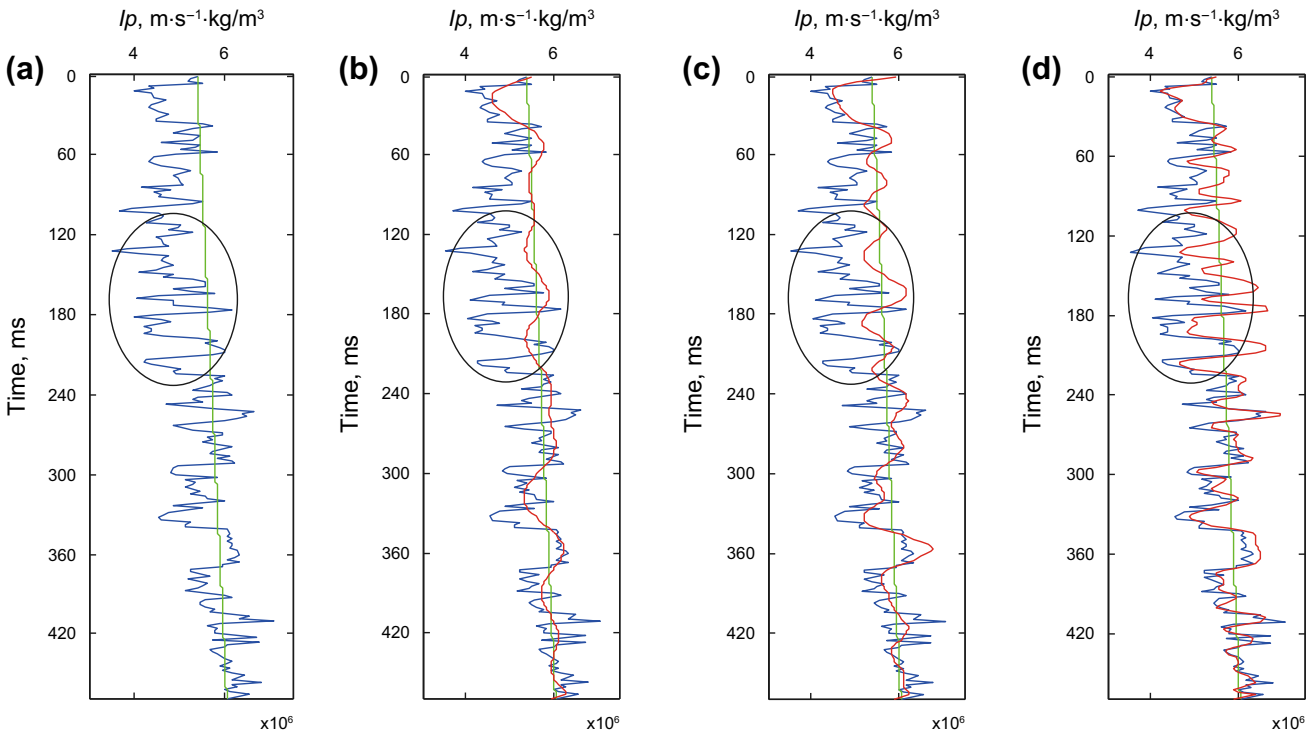

Fig. 5 Estimated parameters without the constraint of low-frequency estimation in Laplace mixed domains under no-noise condition. **a** Initial model, **b** 5.0–15.0 Hz estimation, **c** 5.0–30.0 Hz estimation and **d** 5.0–55.0 Hz estimation. In each figure, blue refers to the original model, green refers to the initial model and red refers to the predicted parameters

mixed-domain inversion performs better than the conventional inversion approach shown in Fig. 5 under no-noise condition and the low-frequency information can be predicted precisely even though the initial model is in linear incremental mode. If seismic gathers were contaminated by random noise, the estimated low frequency was

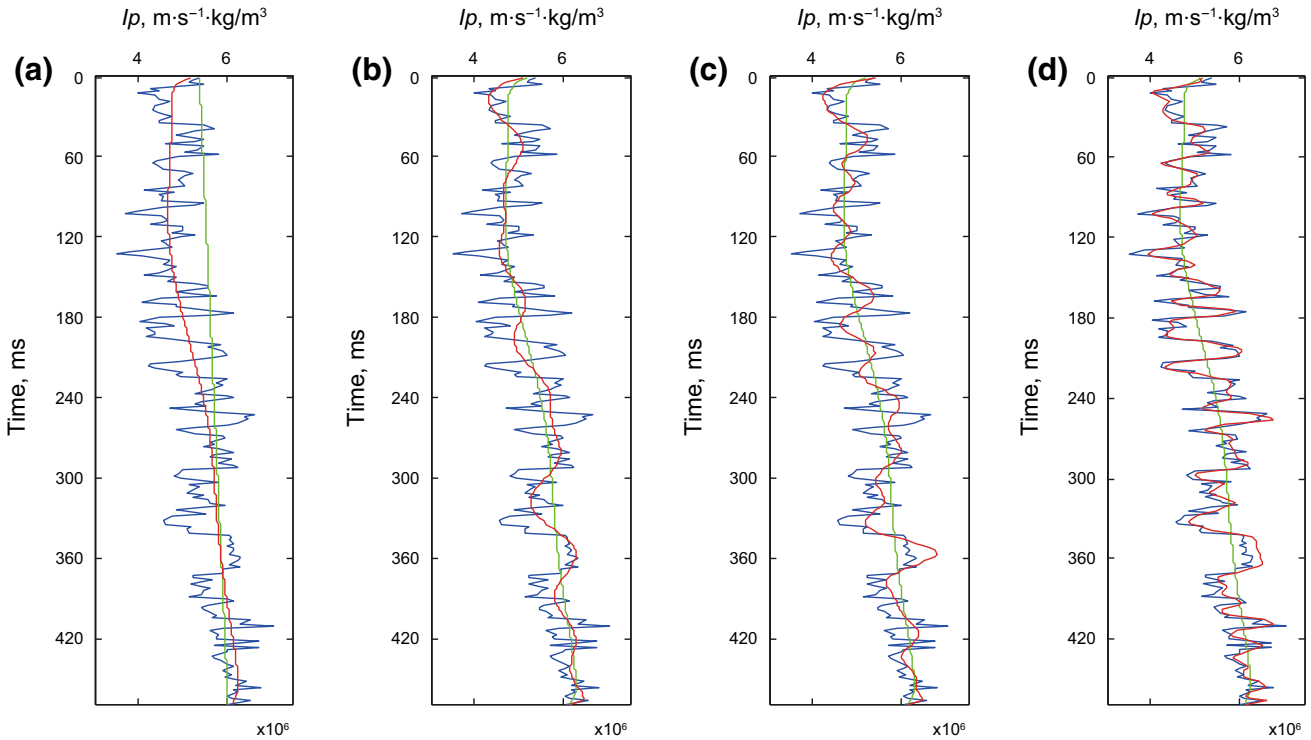

Fig. 6 Estimated parameters with the proposed method in the Laplace mixed domains under no-noise condition, **a** Low-frequency estimation, **b** 5.0–15.0 Hz estimation, **c** 5.0–30.0 Hz estimation and **d** 5.0–55.0 Hz estimation. The inversion process is implemented by successive iterations of multi-frequency components, which means that the previous inverted result is considered as the initial model for the next inversion process

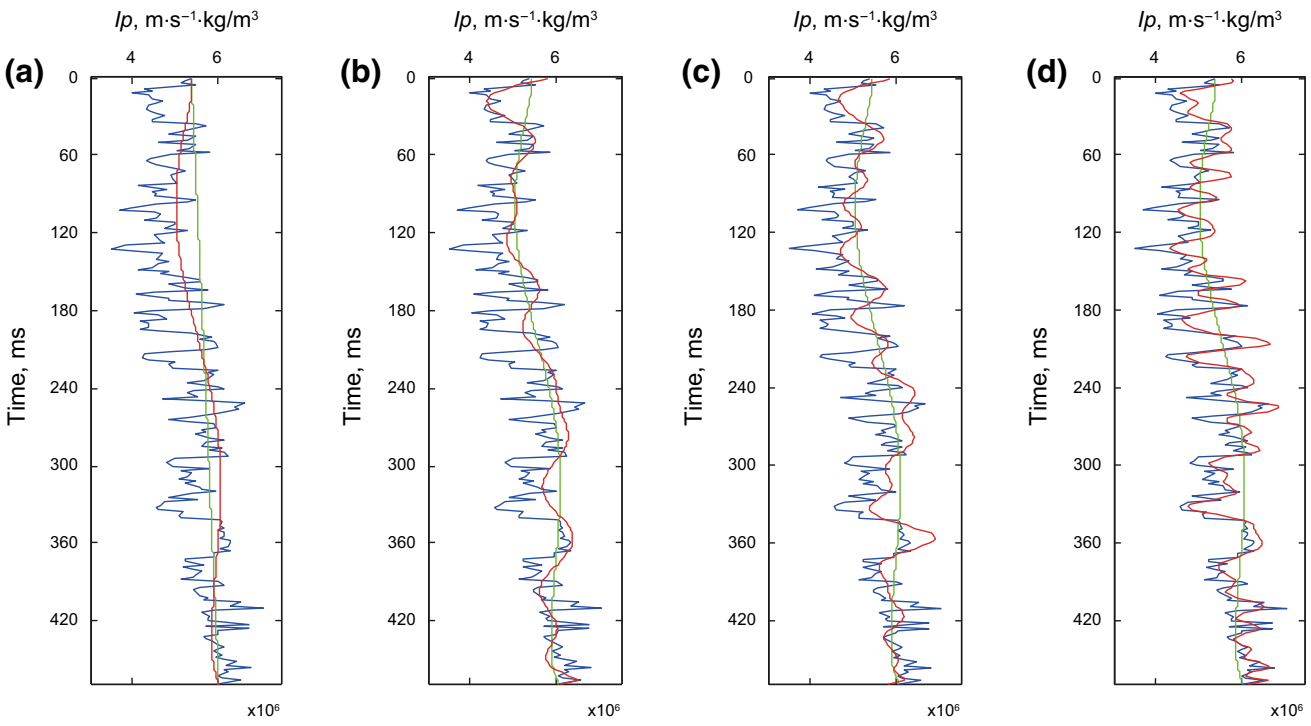

Fig. 7 Estimated parameters with our proposed method in the Laplace mixed domains with $S/N = 20$. **a** Low-frequency estimation, **b** 5.0–15.0 Hz estimation, **c** 5.0–30.0 Hz estimation and **d** 5.0–55.0 Hz estimation

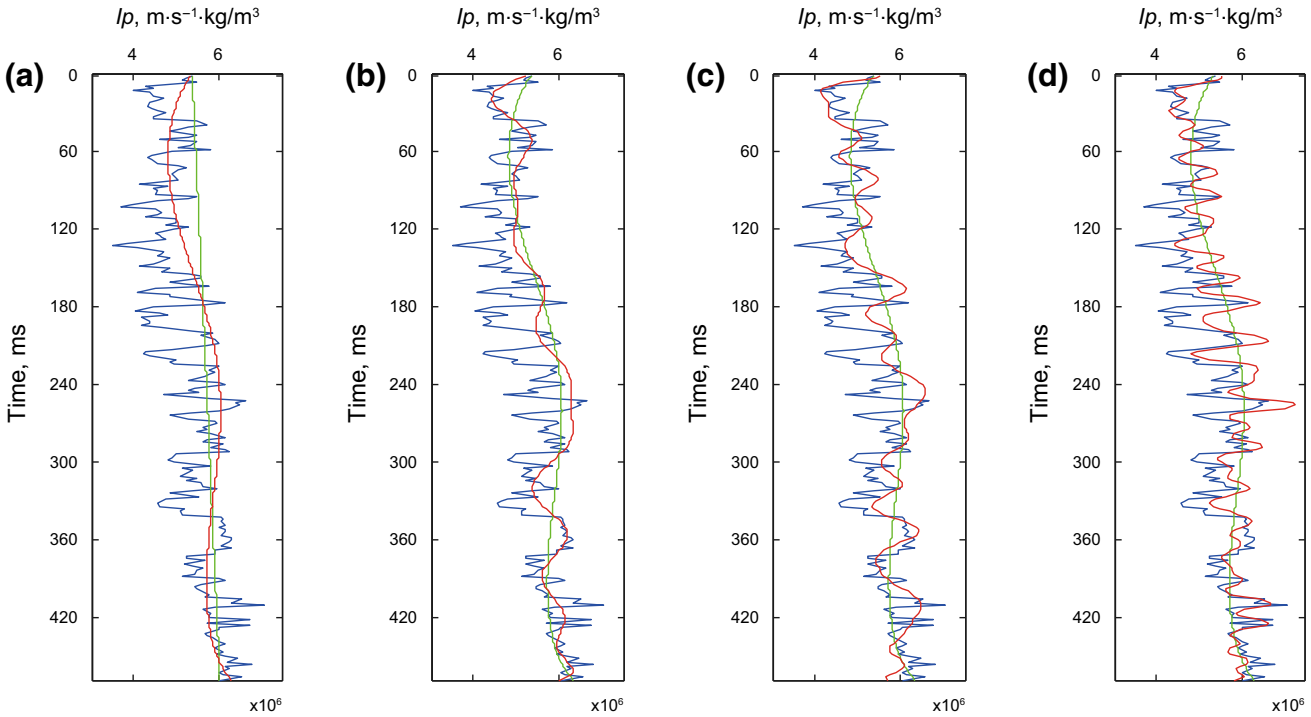

Fig. 8 Estimated parameters with our proposed method in the Laplace mixed domains with $S/N = 10$. **a** Low-frequency estimation, **b** 5.0–15.0 Hz estimation, **c** 5.0–30.0 Hz estimation and **d** 5.0–55.0 Hz estimation

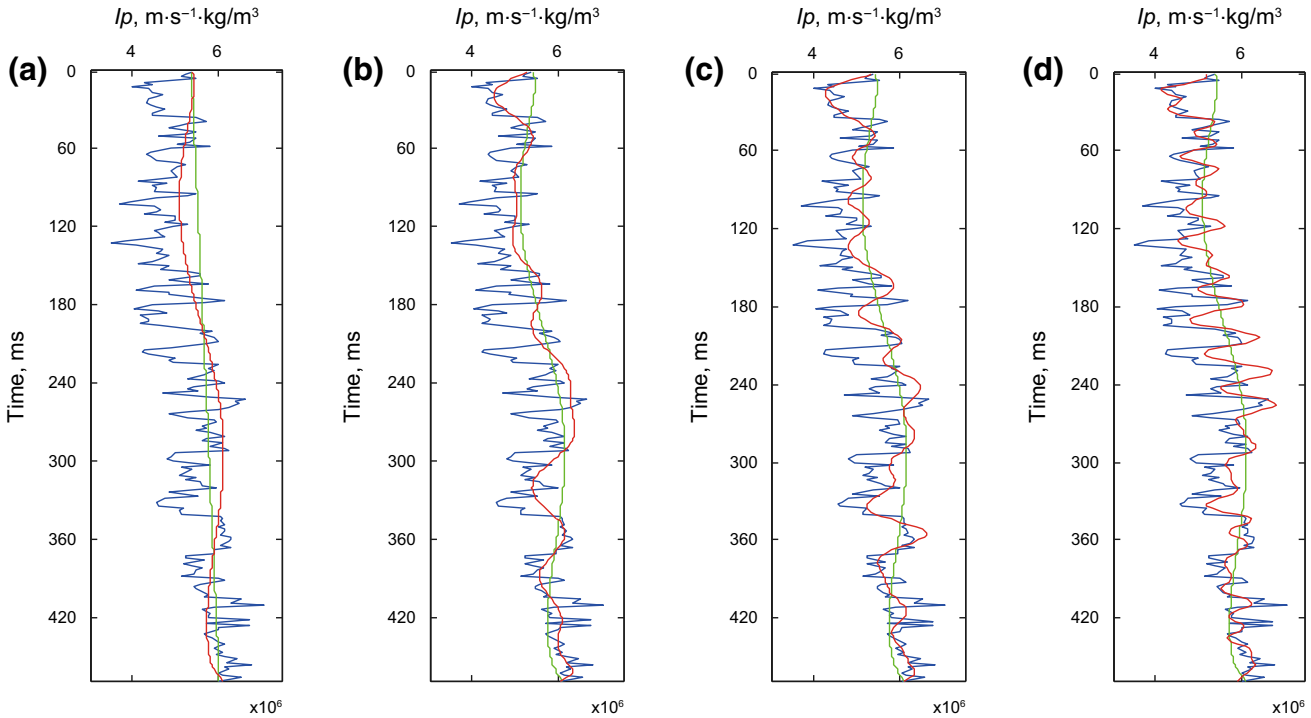

Fig. 9 Estimated parameters with our proposed method in the Laplace mixed domains with $S/N = 5$. **a** Low-frequency estimation, **b** 5.0–15.0 Hz estimation, **c** 5.0–30.0 Hz estimation and **d** 5.0–55.0 Hz estimation

affected but can be accepted with $S/N = 5$ in Fig. 9. With the constraint of low-frequency background, the subsurface parameters can be recovered by multi-scale inversion with multi-component iterations easily, as shown in Figs. 6b–d and 9b–d. The higher consistency with theoretical value verifies the feasibility of the low-frequency estimation and

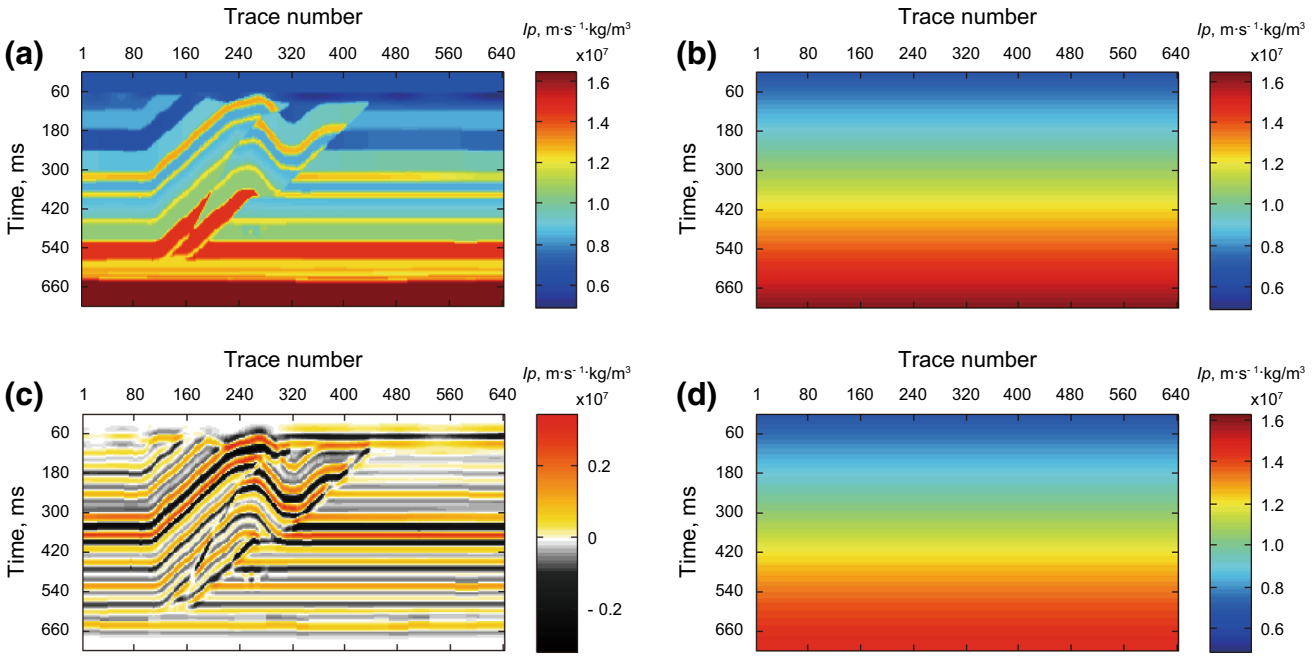

Fig. 10 2D estimated results from the conventional Bayesian impedance inversion method in the pure frequency domain. **a** Overthrust model, **b** initial model, **c** synthetic seismic profile and **d** the estimated result from the conventional Bayesian impedance inversion in the pure frequency domain using 0 Hz and without σ

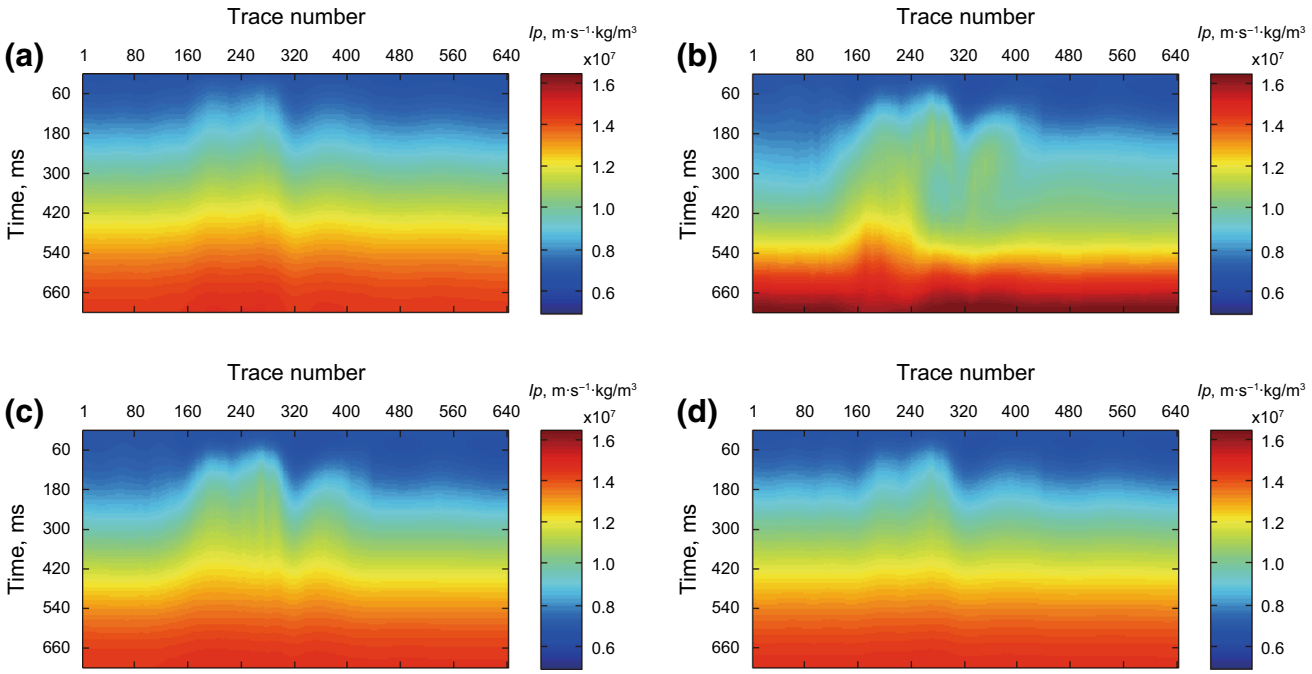

Fig. 11 Estimated 2D results with different Laplace coefficients and different frequency components in the Laplace mixed-domain. **a** Estimated result using 0.0 Hz in the Laplace domain and σ changes from 0 to 10, **b** estimated result using 1.22 Hz and σ changes from 0 to 10, **c** estimated result using 1.22 Hz and σ changes from 10 to 20, and **d** estimated result using 1.22 Hz and σ changes from 20 to 30

progressive optimization Bayesian algorithm in a complex Laplace domain.

5.2 2D synthetic tests

For further verification of the validity and lateral continuity of the proposed method, the overthrust mode in Fig. 10a is utilized to conduct 2D synthetic tests. The synthetic seismic profile shown in Fig. 10c is also obtained from a time-convolution model with a 20-Hz zero-phase Ricker wavelet. The linear incremental model is shown in Fig. 10b, and the lateral value is almost constant. The first step is the estimation of low-frequency background information. Figure 10d demonstrates the estimated result of conventional Bayesian impedance inversion with 0 Hz as the input frequency in the pure frequency domain. It is clear that the conventional inversion method cannot estimate the low-frequency information efficiently. The predicted result is the same as the initial model because there is no input response of 0 Hz (i.e., 0 Hz is equivalent to no input data). Figure 11a–d displays the low-frequency estimated results with different damping coefficients and frequency components. If only zero frequency is considered as the input of the mixed-domain inversion, only the real Laplace spectrum can be used to conduct the low-frequency estimation. Figure 11a shows the predicted result in the pure Laplace domain (only the real part) with the variation of Laplace damping constants from 0 to 10. Comparing Fig. 11a with Fig. 10d, it can be seen that the low-frequency estimation result with Bayesian inversion in the complex Laplace mixed-domain can restore the low-frequency background better than the conventional seismic inversion method. We can conclude that the introduction of the Laplace damping coefficient in the inversion algorithm contributes to the

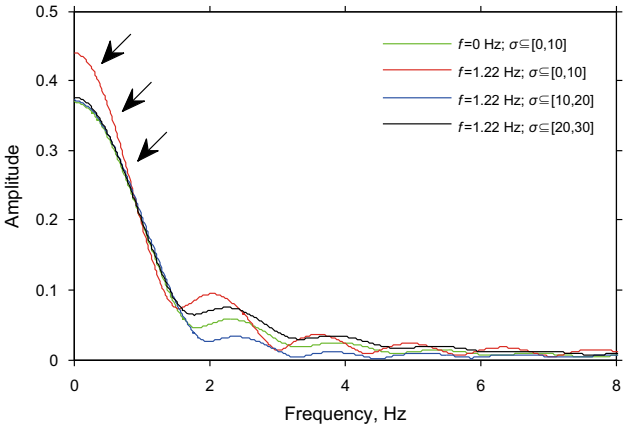

Fig. 13 Amplitude spectrum of estimated low-frequency results in Fig. 12

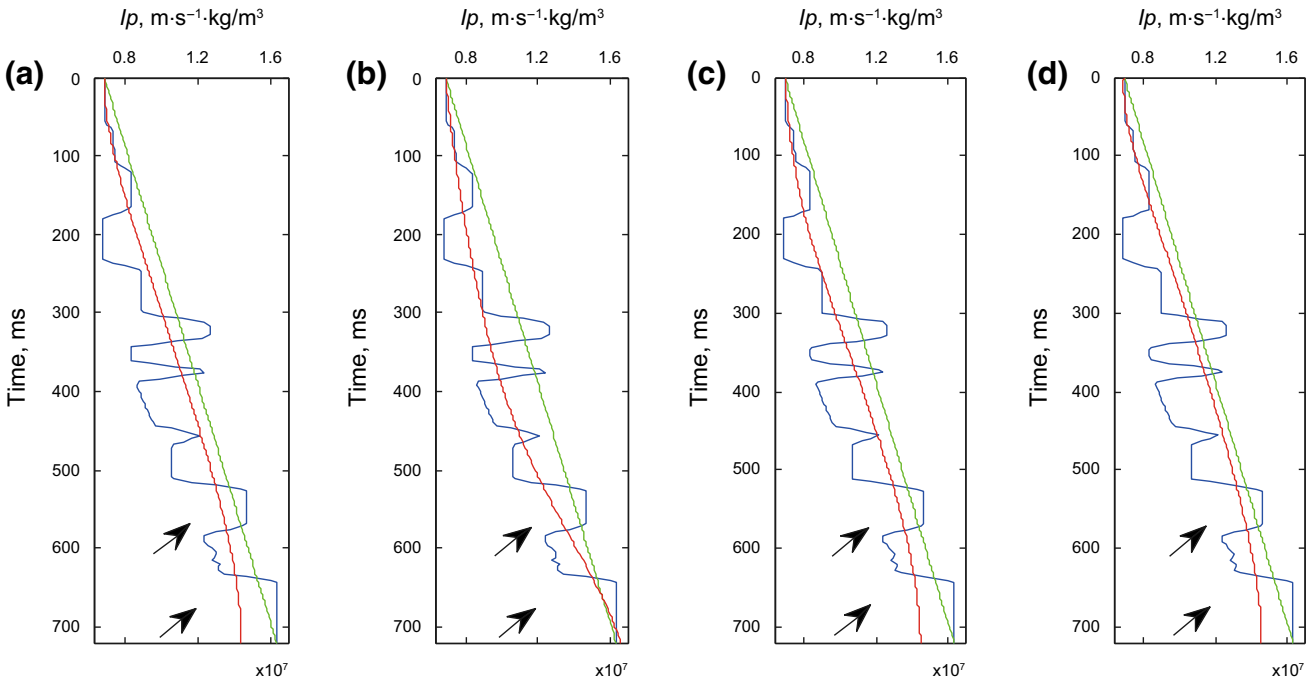

Fig. 12 Extracted low-frequency results corresponding to the first trace from Fig. 11 (blue lines are the real parameters, green lines are initial parameters and red lines are the predicted parameters). **a** Low-frequency result of the first trace from Fig. 11a, **b** low-frequency result of the first trace from Fig. 11b, **c** low-frequency result of the first trace from Fig. 11c and **d** low-frequency result of the first trace from Fig. 11d

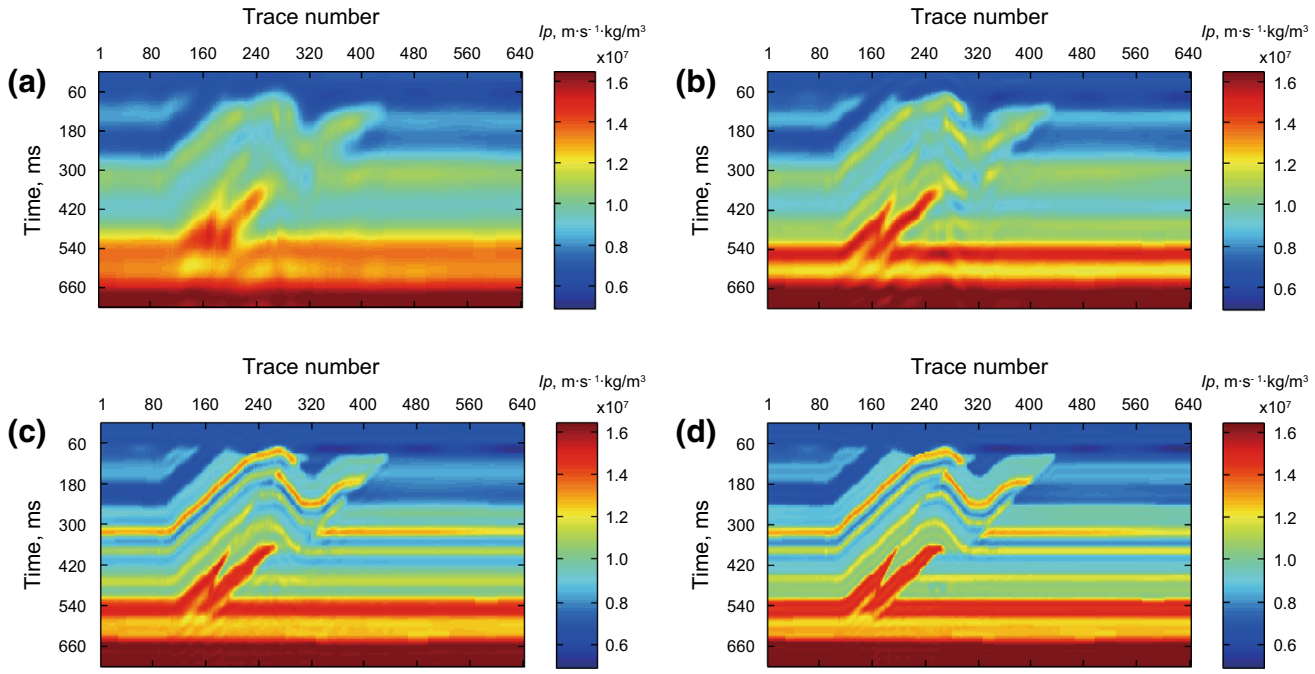

Fig. 14 Final estimated results with different frequency components. **a** 3.17–5.13 Hz, **b** 3.17–10.49 Hz, **c** 3.17–20.51 Hz and **d** 3.17–30.51 Hz

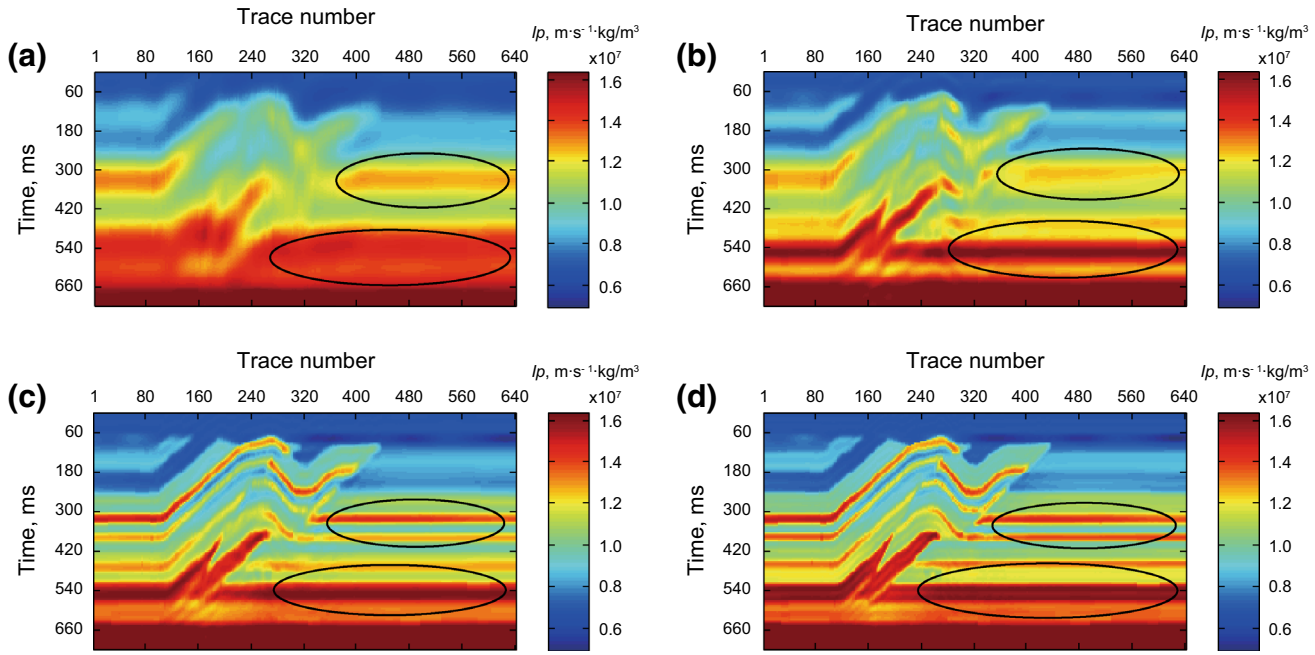

Fig. 15 Estimated results with conventional Bayesian seismic inversion based on the linear incremental model. **a** 3.17–5.13 Hz, **b** 3.17–10.49 Hz, **c** 3.17–20.51 Hz and **d** 3.17–30.51 Hz

recovery of the low-frequency response, which is consistent with the theoretical analysis in Figs. 2 and 3.

To show the influence of frequency selection on the proposed method, 1.22 Hz with real and imaginary spectra of damped seismic data is taken into account, which can yield more reliable low-frequency information, as shown in Fig. 11b. Different Laplace damping constants can also affect the penetration depth of the Laplace mixed-domain impedance inversion, as shown in Fig. 11c–d. Figure 11c shows that the predicted result of 1.22 Hz as damping constants varies from 10 to 20. Figure 11d demonstrates the predicted result with the variation of damping constants

from 20 to 30. The estimated low-frequency results and spectrum of the first trace from Fig. 11 are shown in Figs. 12 and 13, respectively. It is clear that deeper background and low-frequency components of estimated parameters can be recovered better with 1.22 Hz and σ ranging from 0 to 10, especially at the location of the black arrows. There are two principles for the selection of low-frequency components. First, the input low frequency of

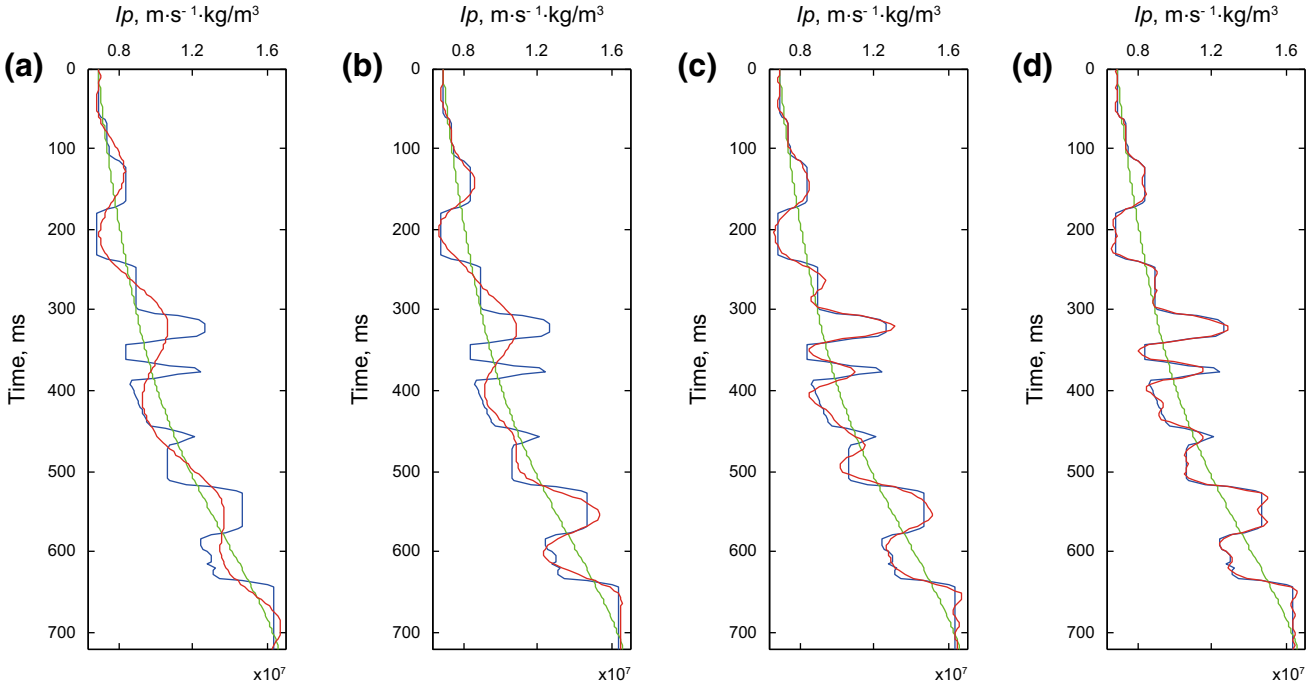

Fig. 16 Predicted results of the first trace corresponding to different frequency components extracted from profiles in Fig. 14. **a** 3.17–5.13 Hz, **b** 3.17–10.49 Hz, **c** 3.17–20.51 Hz and **d** 3.17–30.51 Hz

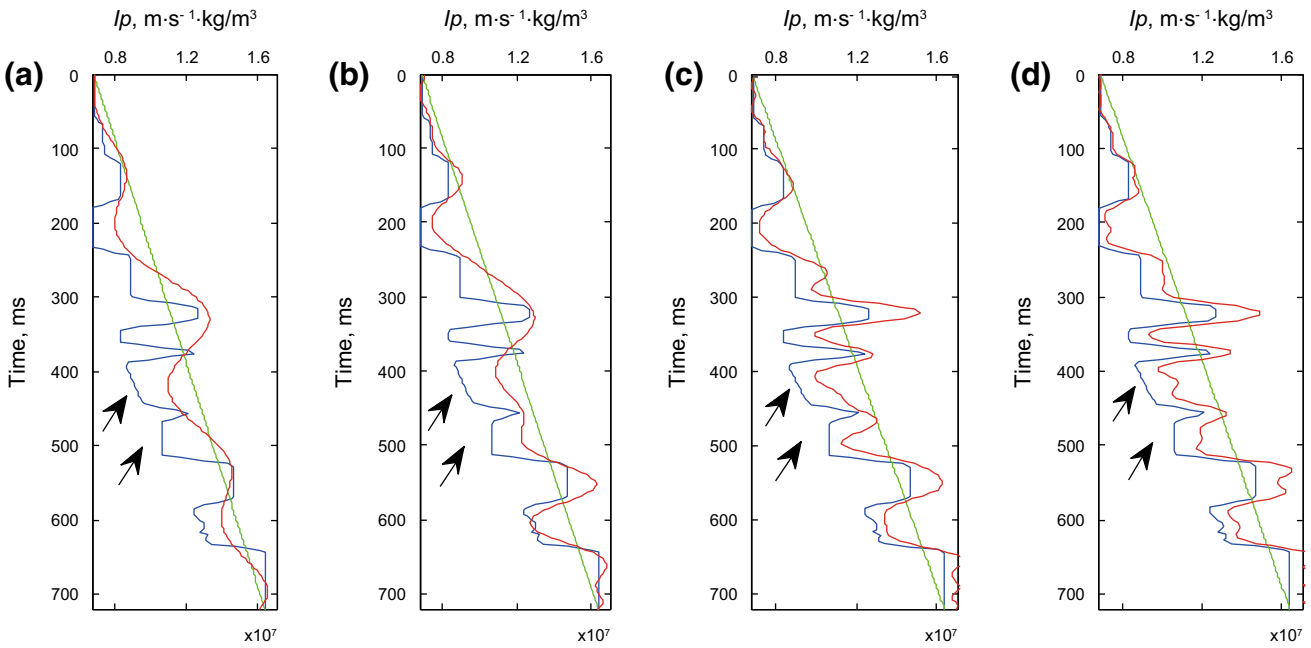

Fig. 17 Predicted results of the first trace corresponding to different frequency components extracted from profiles in Fig. 15. **a** 3.17–5.13 Hz, **b** 3.17–10.49 Hz, **c** 3.17–20.51 Hz and **d** 3.17–30.51 Hz

Laplace mixed inversion should always be limited to 0–5 Hz in the first stage. Besides, increasing the frequency up to 5 Hz appropriately and inputting some indispensable small attenuation coefficients can improve the reliability of low-frequency estimation. Second, the selection of low frequency should be combined with the multi-scale decomposition of borehole-side seismic. And according to the scale divisions of low-frequency components, we can determine the specific low-frequency components required for large-scale background of elastic parameters (Cao et al. 2009; Yang and Wu 2016).

The next step is frequency-domain inversion by multi-component successive iterations, which means that the previous estimated result is considered as the initial model for the next inversion procedure. Besides, the low-frequency result in Fig. 11b is the initial model of the first inversion iteration. Figure 14a–d shows the final estimated impedance profiles of 3.17–5.13, 3.17–10.49, 3.17–20.51 and 3.17–30.51 Hz. We can see that the lateral continuity and low-frequency background of the model parameter can be preserved successfully. However, the estimated results based on the constraint of a linear incremental model with conventional Bayesian seismic inversion are displayed in Fig. 15, and there are many errors on the low-frequency background of the final estimated impedance with conventional seismic inversion, as can be seen especially at the black ellipses. To evaluate the estimated result more clearly, the impedance of the first trace from Figs. 14 and 15 is displayed in Figs. 16 and 17. As expected, we see that the proposed multi-scale inversion can achieve more reliable and superior resolution results incorporating the estimated low-frequency background from Laplace mixed-domain inversion than conventional Bayesian inversion.

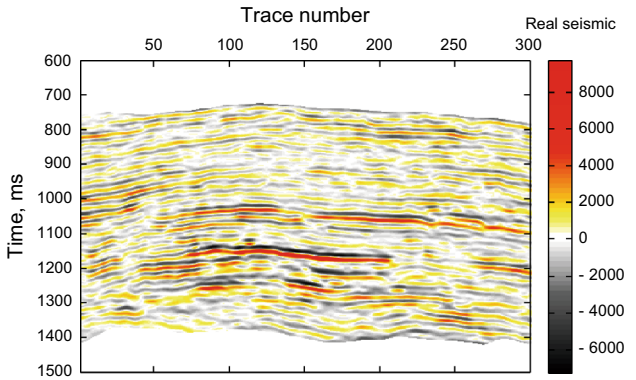

Fig. 18 One real broadband seismic profile collected from the SL exploration area in east of China

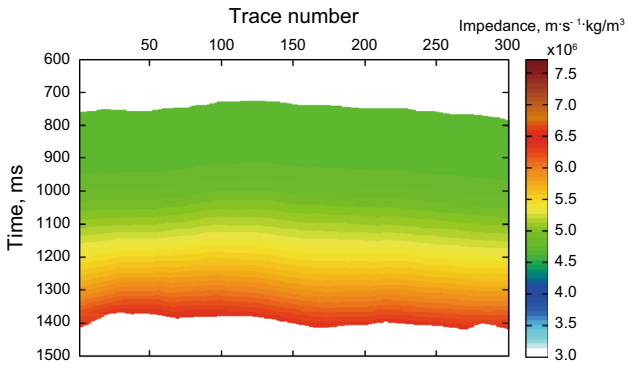

Fig. 19 Initial linear impedance model established by well interpolation; there is no variation in the lateral direction

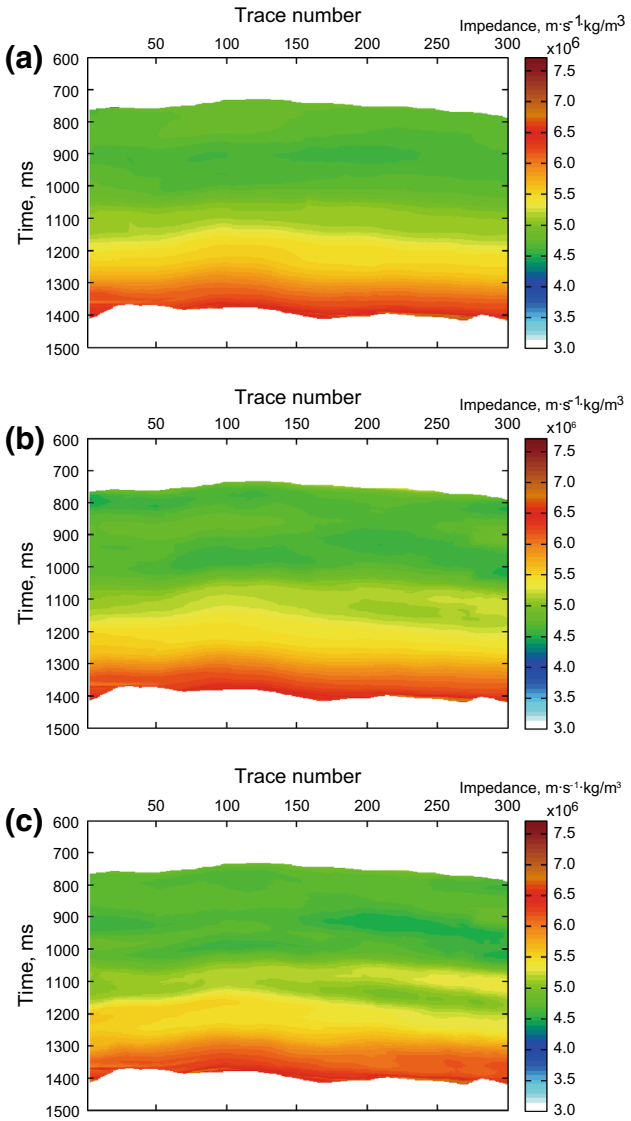

Fig. 20 Estimated results of the low-frequency model with Laplace mixed-domain inversion and different input parameters: **a** the input frequency components are 0–2.93 Hz and the damping constants σ change from 0 to 5, **b** the input frequency components are 0–5.37 Hz and the damping constants σ change from 4 to 10, and **c** the input frequency components are 0–5.37 Hz and the damping constants σ change from 0 to 5

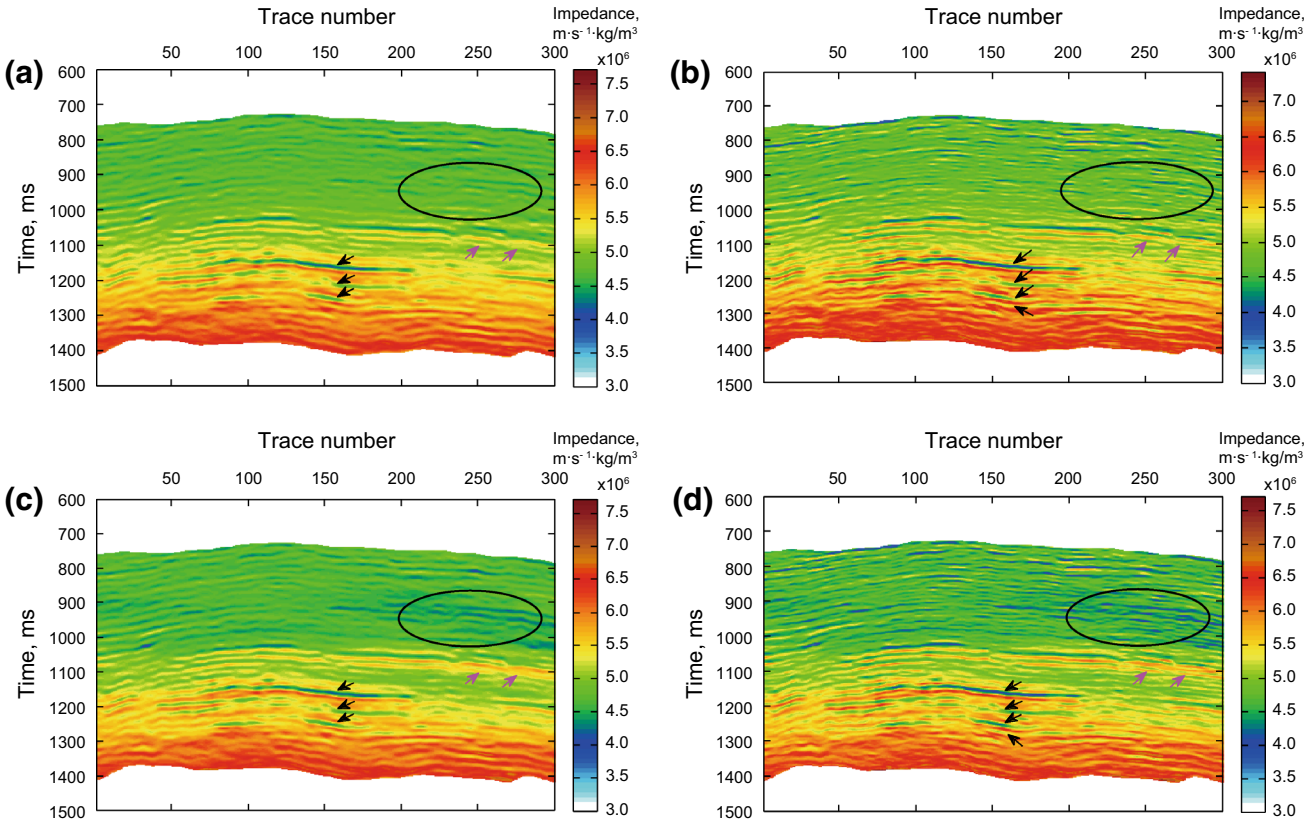

Fig. 21 The final estimated results of multi-scale inversion in frequency domain: **a** estimated result with conventional frequency-domain Bayesian inversion and initial linear model constraint in Fig. 19, **b** estimated impedance with multi-scale Bayesian inversion in the frequency domain and initial linear model constraint in Fig. 19, **c** estimated result with conventional frequency-domain Bayesian inversion and low-frequency estimation constraint in Fig. 20c, **d** estimated result with multi-scale Bayesian inversion in the frequency domain and low-frequency estimation constraint in Fig. 20c

6 Field data results

The proposed method was illustrated with 1D and 2D synthetic tests to verify the feasibility and lateral continuity of inversion results. However, the real seismic profile is always contaminated by random noise, especially for the low-frequency components. To demonstrate the practicability of our method, one real broadband case from the east of China is studied in this paper. One real broadband seismic profile collected from the SL oilfield is displayed in Fig. 18, and the band of effective frequency is 3.0–78.0 Hz.

Figure 19 shows the initial linear model established by well interpolation, and there is no variation along the horizontal direction. This linear increment mode is the input constraint of our Laplace mixed-domain inversion. Figure 20a–c illustrates the estimated results of the ultra-low-frequency information incorporating different frequency components and Laplace damping constants. Figure 20a–c shows the low-frequency estimation results using 0–2.93 Hz and the damping constants σ from 0 to 5, 0–5.37 Hz and damping constants σ from 4 to 10, 0–5.37 Hz and damping constants σ from 0 to 5, respectively. Comparing the low-frequency estimation results in Fig. 20, we can see that the low-frequency result in Fig. 20c behaves better than in Fig. 20a, b, and if input frequency components are insufficient and Laplace coefficients have a deficiency of low constants, it becomes difficult to recover the low-frequency structure accurately.

As such, the predicted result in Fig. 20c is considered as the initial model of next multi-scale inversion in the frequency domain. According to the effective frequency band of seismic data of 3.0–78.0 Hz, the selections of frequency ranges in multi-scale inversion are 5.0–12.0, 12.0–32.0, 32.0–60.0 and 60.0–75.0 Hz. To demonstrate the importance of low frequency in seismic inversion, the final estimated results are displayed in Fig. 21a–d with different initial models and different inversion methods. Under the linear model constraint shown in Fig. 19, the estimated

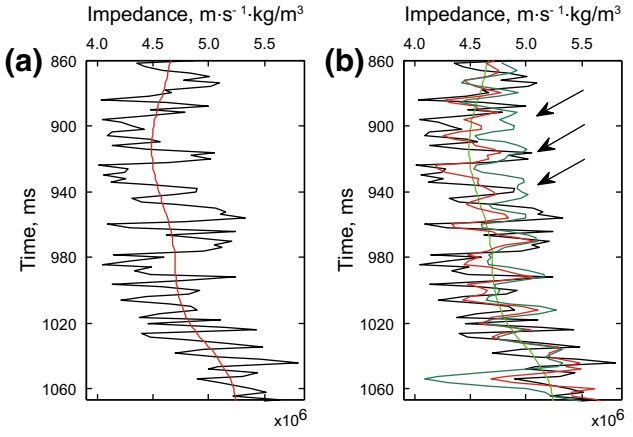

Fig. 22 Extracted borehole-side results from Figs. 20 and 21 (black is the resampling well-logging data, red is the estimated results with proposed method from Fig. 20c and Fig. 21d, green is the low-frequency constraints and dark green is the estimated results with conventional multi-scale inversion from Fig. 21b). **a** Low-frequency results and **b** final estimated results

results with conventional Bayesian inversion and multi-scale Bayesian inversion in the frequency domain are shown in Fig. 21a, b. If the low-frequency result in Fig. 20c is taken as the background constraint of seismic inversion, the estimated results with conventional Bayesian inversion and the proposed multi-scale Bayesian inversion are shown in Fig. 21c, d, respectively. For the resolution of the seismic inversion algorithm, we can see from Fig. 21a, b that multi-scale Bayesian inversion in the frequency domain can achieve better resolution than conventional Bayesian inversion, specifically shown at red arrows and black ellipses. Similarly, the same conclusion can be deduced from Fig. 21c, d. Most of all, the final impedance result in Fig. 21d can discriminate the four lithologic reservoirs more obviously at the four black arrows than the estimated results with conventional inversion method in Fig. 21a, c.

Besides, the other major differences occurred in the black ellipses that the phenomena of relative low impedance in Fig. 21c, d disappeared in Fig. 21a, b, which can be explained that the initial linear model is insufficient for recovering accurate information of the underground model. In Fig. 22, we can see clearly that the borehole-side results at CDP 220 would have a better estimation with the low-frequency constraint than the conventional multi-scale inversion, especially at the three black arrows. Thus, this adequate proof illustrates that the proposed Bayesian multi-scale inversion in Laplace mixed domains not only enhances the low-frequency reliability, but also improves the resolution of the inversion.

7 Conclusions

To remove the model dependence problem of seismic inversion, the novel Bayesian multi-scale inversion in the Laplace mixed domains is elaborated to enhance the ultra-low-frequency information of subsurface models. The object function of inversion can be established to improve the stability, which relies on the Bayesian system and the linear increment model. Furthermore, the feasibility of Laplace mixed-domain impedance inversion is demonstrated by 1-D synthetic tests under different noise levels. The tests show that our proposed method is capable of obtaining stable results with $S/N > 5$. In addition, applications on the 2-D overthrust model illustrate the lateral continuity and reliability of the inversion results. In comparison with the inversion results of different input parameters, we found that low Laplace damping constants are essential to excavate the low-frequency background of deeper subsurface structures. Besides, the input frequency components (less than 5 Hz) of the damped wave field should be raised appropriately to enhance the input spectrum energy. One field case from the east of China demonstrates the practicability and potential of Laplace–Fourier impedance inversion. By analyzing the resolution characteristics of different inversion methods, the results illustrate that multi-scale inversion in frequency domain can achieve superior resolution with the help of low-frequency estimation results, as predicted by the Laplace mixed-domain inversion.

Acknowledgements We would like to acknowledge the sponsorship of National Natural Science Foundation Project (U1562215, 41604101), National Grand Project for Science and Technology (2016ZX05024-004, 2017ZX05032-003), the Post-graduate Innovation Program of China University of Petroleum (YCX2017005), Science Foundation from SINOPEC Key Laboratory of Geophysics (wtyjy-wx2016-04-10) and the Fundamental Research Funds for the Central Universities.

References

Alemie W, Sacchi M. High-resolution three-term AVO inversion by means of a Trivariate Cauchy probability distribution. Geophysics. 2011;76(3):R43–55. doi:10.1190/1.3554627.

Buland A, Omre H. Bayesian linearized AVO inversion. Geophysics. 2003;68(1):185–98. doi:10.1190/1.1543206.

Cao SH, Chen JB. Studies on complex frequencies in frequency domain full waveform inversion. Chin J Geophys. 2014;57(7):2302–13. doi:10.6038/cjg20140724 **(in Chinese)**.

Cao DP, Yin XY, Zhang FC, et al. A study on the method of joint inversion of multiscale seismic data. Chin J Geophys. 2009;52(4):1059–67. doi:10.3969/j.issn.01-5733.2009.04.023 **(in Chinese)**.

Chabyshova E, Goloshubin G. Seismic modeling of low-frequency "shadows" beneath gas reservoirs. Geophysics. 2014;79(6): D417–23. doi:10.1190/geo2013-0379.1.

Chen XH, He ZH, Zhu SX, et al. Seismic low-frequency-based calculation of reservoir fluid mobility and its applications. Appl Geophys. 2012;9(3):326–32. doi:10.1007/s11770-012-0340-6.

Day A, Klüver T, Söllner W, et al. Wavefield-separation methods for dual-sensor towed-streamer data. Geophysics. 2013;78(2): WA55–70. doi:10.1190/geo2012-0302.1.

Downton JE. Seismic parameter estimation from AVO inversion. Ph.D. Thesis, University of Calgary. 2005.

Haavik KE, Landrø M. Variable source depth acquisition for improved marine broadband seismic data. Geophysics. 2015;80(3):A69–73. doi:10.1190/geo2014-0437.1.

Hu Y, Zhang D, Yuan J, et al. An efficient multi-scale waveform inversion method in Laplace–Fourier domain. Pet Explor Dev. 2015;42(3):369–78. doi:10.1016/s1876-3804(15)30027-6.

Ha W, Shin C. Laplace-domain full-waveform inversion of seismic data lacking low-frequency information. Geophysics. 2012;77(5):R199–206. doi:10.1190/geo2011-0411.1.

Ha W, Shin C. Why do Laplace-domain waveform inversions yield long-wavelength results? Geophysics. 2013;78(4):R167–73. doi:10.1190/geo2012-0365.1.

Hamid H, Pidlisecky A. Multitrace impedance inversion with lateral constraints. Geophysics. 2015;80(6):M101–11. doi:10.1190/geo2014-0546.1.

Kim HJ, Kim YH. A unified transformation function for lower and upper bounding constraints on model parameters in electrical and electromagnetic inversion. J Geophys Eng. 2011;8(1):21–6. doi:10.1088/1742-2132/8/1/004.

Kroode FT, Bergler S, Corsten C, et al. Broadband seismic data—the importance of low frequencies. Geophysics. 2013;78(2):WA3–14. doi:10.1190/geo2012-0294.1.

Luo JR, Wu RS. Seismic envelope inversion: reduction of local minima and noise resistance. Geophys Prospect. 2015;63(3): 597–614. doi:10.1111/1365-2478.12208.

Luo JR, Wu RS, Gao JH. Local minima reduction of seismic envelope inversion. Chin J Geophys. 2016;59(7):2510–8. doi:10.6038/cjg20160716 **(in Chinese)**.

Li K, Yin XY, Zong ZY. Seismic multi-scale inversion in the frequency domain based on a smooth model constraint. Oil Geophys Prospect. 2016a;51(4):760–8. doi:10.13810/j.cnki.issn.1000-7210.2016.04.018 **(in Chinese)**.

Li K, Yin XY, Zong ZY. Time frequency domain FAVO fluid discrimination method based on matching pursuit spectrum decomposition. Acta Pet Sin. 2016b;37(6):777–86. doi:10.7623/syxb201606008 **(in Chinese)**.

Liu ZW, Wang YC, Zhao HX, et al. High-resolution processing methods of thin interbeds imaging. Chin J Geophys. 2013;56(4):1350–9. doi:10.6038/cjg20130429 **(in Chinese)**.

Liu XJ, Yin XY, Wu GC, et al. Identification of deep reservoir fluids based on basis pursuit inversion for elastic impedance. Chin J Geophys. 2016;59(1):277–86. doi:10.6038/cjg20160123 **(in Chinese)**.

Margrave G. Theory of nonstationary linear filtering in the Fourier domain with application to time-variant filtering. Geophysics. 1998;63(1):244–59. doi:10.1190/1.1444318.

Pedersen L, Becken M. Equivalent images derived from very-low-frequency (VLF) profile data. Geophysics. 2005;70(3):G43–50. doi:10.1190/1.1925742.

Shin C, Cha YH. Waveform inversion in the Laplace domain. Geophys J Int. 2008;173(3):922–31. doi:10.1111/j.1365-246x.2008.03768.x.

Shin C, Cha YH. Waveform inversion in the Laplace–Fourier domain. Geophys J Int. 2009;177(3):1067–79. doi:10.1111/j.1365-246x.2009.04102.x.

Sirgue L, Pratt RG. Efficient waveform inversion and imaging: A strategy for selecting temporal frequencies. Geophysics. 2004;69(1):231–48. doi:10.1190/1.1649391.

Spjuth C, Sabel PB, Foss SK, et al. Broadband seismic for sub-basalt Exploration. In: 74th annual international meeting, EAGE, expanded abstract. 2012. doi:10.3997/2214-4609.20148151.

Tarantola A. Inverse problem theory and methods for model parameter estimation. Soc Ind Appl Math. 2005;9:1597–620. doi:10.1137/1.9780898717921.

Wu RS, Luo JR, Wu BY. Seismic envelope inversion and modulation signal model. Geophysics. 2014;79(3):WA13–24. doi:10.1190/geo2013-0294.1.

Yang PJ. Seismic wavelet blind extraction and non-linear inversion. Ph.D. thesis. China University of Petroleum. 2008 **(in Chinese)**.

Yang QL, Wu GC. Multi-scale seismic inversion method based on Bayesian theory. Prog Geophys. 2016;31(3):1246–56. doi:10.6038/pg20160343 **(in Chinese)**.

Yang PJ, Wang CJ, Bi JF, et al. Direct extraction of the fluid factor based on variable point-constraint. Chin J Geophys. 2015;58(6):2188–200. doi:10.6038/cjg20150631 **(in Chinese)**.

Yuan SY, Wang SX. Spectral sparse Bayesian learning reflectivity inversion. Geophys Prospect. 2013;61(4):735–46. doi:10.1111/1365-2478.12000.

Yin XY, Zong ZY, Wu GC. Improving seismic interpretation: a high-contrast approximation to the reflection coefficient of a plane longitudinal wave. Pet Sci. 2013;10(4):466–76. doi:10.1007/s12182-013-0297-y.

Yin XY, Zong ZY, Wu GC. Research on seismic fluid identification driven by rock physics. Sci China Earth Sci. 2015a;58(2):159–71. doi:10.1007/s11430-014-4992-3.

Yin XY, Liu XJ, Zong ZY. Pre-stack basis pursuit seismic inversion for brittleness of shale. Pet Sci. 2015b;12(4):618–27. doi:10.1007/s12182-015-0056-3.

Yin XY, Li K, Zong ZY. Resolution enhancement of robust Bayesian pre-stack inversion in the frequency domain. J Geophys Eng. 2016;13(5):646–56. doi:10.1088/1742-2132/13/5/646.

Zhang R, Sen MK, Srinivasan S. A prestack basis pursuit seismic inversion. Geophysics. 2013;78(1):R1–11. doi:10.1190/geo2011-0502.1 **(in Chinese)**.

Zhang Z, Yin XY, Hao QY. Frequency-dependent fluid identification method based on AVO inversion. Chin J Geophys. 2014;57(12):4171–84. doi:10.6038/cjg20141228.

Zhang JH, Zhang BB, Zhang ZJ, et al. Low-frequency data analysis and expansion. Appl Geophys. 2015;12(2):212–20. doi:10.1007/s11770-015-0484-2.

Zong ZY, Yin XY, Zhang F, et al. Reflection coefficient Equation and pre-stack seismic inversion with Young's modulus and Poisson ratio. Chin J Geophys. 2012;55(11):3786–94. doi:10.6038/j.issn.0001-5733.2012.11.025 **(in Chinese)**.

Zong ZY, Yin XY, Wu GC. Geofluid discrimination incorporating poroelasticity and seismic reflection inversion. Surv Geophys. 2015;36(5):659–81. doi:10.1007/s10712-015-9330-6.

Zong ZY, Yin XY, Li K. Joint AVO inversion in the time and frequency domain with Bayesian interference. Appl Geophys. 2016;13(4):631–40. doi:10.1007/s11770-016-0584-7.